 doi:10.20944/preprints202207.0043.v1

THz filters made by laser ablation of stainless steel and kapton

Molong Han,[1] Daniel Smith,[1] Soon Hock Ng,[1,2] Zoltan Vilagosh,[1] Vijayakumar Anand,[3] Tomas Katkus,[1] Ignas Reklaitis,[4] Haoran Mu,[1] Meguya Ryu,[5] Junko Morikawa,[6,7] Jitraporn Vongsvivut,[8] Dominique Appadoo,[9] and Saulius Juodkazis[1,6]

[1)] *Optical Sciences Centre and ARC Training Centre in Surface Engineering for Advanced Materials (SEAM), School of Science, Swinburne University of Technology, Hawthorn, Vic 3122, Australia*[a)]

[2)] *Melbourne Centre for Nanofabrication, 151 Wellington Road, Clayton Vic 3168, Australia*

[3)] *Institute of Physics, University of Tartu, 50411, Tartu, Estonia*

[4)] *Institute of Photonics and Nanotechnology, Vilnius University, Saulėtekio ave. 3, 10257, Vilnius, Lithuania*

[5)] *National Metrology Institute of Japan (NMIJ), National Institute of Advanced Industrial Science and Technology (AIST), Tsukuba Central 3, 1-1-1 Umezono, Tsukuba 305-8563, Japan*

[6)] *WRH Program International Research Frontiers Initiative (IRFI) Tokyo Institute of Technology, Nagatsuta-cho, Midori-ku, Yokohama, Kanagawa 226-8503 Japan*

[7)] *CREST-JST and School of Materials and Chemical Technology, Tokyo Institute of Technology, Ookayama, Meguro-ku, Tokyo 152-8550, Japan*

[8)] *ANSTO - Australian Synchrotron, Infrared Microspectroscopy (IRM) Beamline, 800 Blackburn Road, Clayton, Victoria 3168, Australia*

[9)] *ANSTO - Australian Synchrotron, THz/Far-IR Beamline, 800 Blackburn Road, Clayton, Victoria 3168, Australia*

(Dated: 30 June 2022)

THz band-pass filters were fabricated by laser ablation of micro-foils of stainless steel and Kapton. Their spectral performance was tested in transmission and reflection at the THz beamline at the Australian Synchrotron (AuSy). A 25 μm Kapton film performed as a Fabry-Pérot etalon with a free spectral range of $FSR = 119$ cm^{-1}, high finesse $F_c \approx 17$, and was tuneable over ~ 10 μm (at ~ 5 THz band) with $\beta = 30°$ tilt. The structure of the THz beam focal region as extracted by the first mirror (slit) shows a complex polarisation-wavelength-position dependence across the beam. This is important for polarisation sensitive measurements (in transmission and reflection) and requires normalisation at each orientation of linear polarisation.

Keywords: THz filters, synchrotron

I. INTRODUCTION

The spectral range is extremely broad (1 μm-to-1 mm in wavelength) available at the THz beamline and as such, there is a lack of available spectral filters and optical elements to control polarisation – spin angular momentum (SAM) as well as orbital angular momentum (OAM) of this very broadband radiation. In some bio-medical applications, it is imperative to distinguish which part of the IR-THz radiation has effect due to stronger absorption. This is particularly important for beams carrying SAM and OAM since their absorption is dependent on microscopic structure as well as the chirality of constituent

[a)] M. H. and D. S. contributed equally.

Preprints (www.preprints.org) | NOT PEER-REVIEWED | Posted: 4 July 2022 doi:10.20944/preprints202207.0043.v1

molecules/compounds. Before design and fabrication of the required optical elements (filter, polariser, and waveplate), it is useful to carry out proof-of-concept prototyping experiments. The key motivation of this study was to carry out such tests using a simple laser ablation fabrication method for THz band-pass filters[1–4], which have high transmission. The optical elements were tested at the Australian Synchrotron (AuSy) THz/Far-IR beamline after the radiation extraction mirror (the first mirror) was changed, and the optical path realigned for best performance in January 2022 (Fig. 1(a,b)). A detailed analysis of wavelength and polarisation over the cross section of incident synchrotron radiation is important, especially for the emerging application of 3D polarisation tomography using near-fields with the attenuated total reflection (ATR) apparatus for characterising biological samples at the IR-to-THz energies[5]. Polarisation and wavelength composition at the focus has a complex structure, mainly because the synchrotron is not a point like source but has longitudinal dimensions, which has additional complexity due to magnetic field contributions of the Edge Radiation (ER) and Bend Magnet Radiation (BMR)resulting from different locations of the bending trajectories of electrons[6] (see Supplement for additional information based on the 1st mirror used since first light in 2007). Polarisation has a composition of linear $\sim 22\%$ and circular 78% polarisation's due to contributions of the BMR and ER radiation, respectively, as determined earlier for this THz beamline for a broad spectral range[6].

Both the absorption coefficient and the refractive index of water and biological tissues are dominated by water, undergoing significant changes in the wavenumbers $\tilde{\nu} = 20$ to 600 cm^{-1} (0.6 to 18 THz) region. The refractive index reduces from $n \sim 2.19$ at $\tilde{\nu} = 20$ cm^{-1}, to $n \sim 1.33$ at 600 cm^{-1}, with the absorption coefficient increasing from $\alpha \sim 175$ cm^{-1} at $\tilde{\nu} = 20$ cm^{-1} to $\alpha \sim 3200$ cm^{-1} at 600 cm^{-1} at room temperature; the absorption coefficient $\alpha = 4\pi\kappa/\lambda$ where κ is the imaginary part of the refractive index $\tilde{n} = n + i\kappa$ (permittivity ε is $\tilde{n} \equiv \sqrt{\varepsilon}$). The optical density OD is defined as $e^{-\alpha d} = 10^{-OD}$ for a sample of thickness d ($OD = \alpha d/\ln 10$). The rapid change in water properties presents a challenge as varying frequencies have vastly different tissue penetration properties defined by the skin depth $\delta_s = 1/\alpha$. This complicates the assessment of thermal and non-thermal

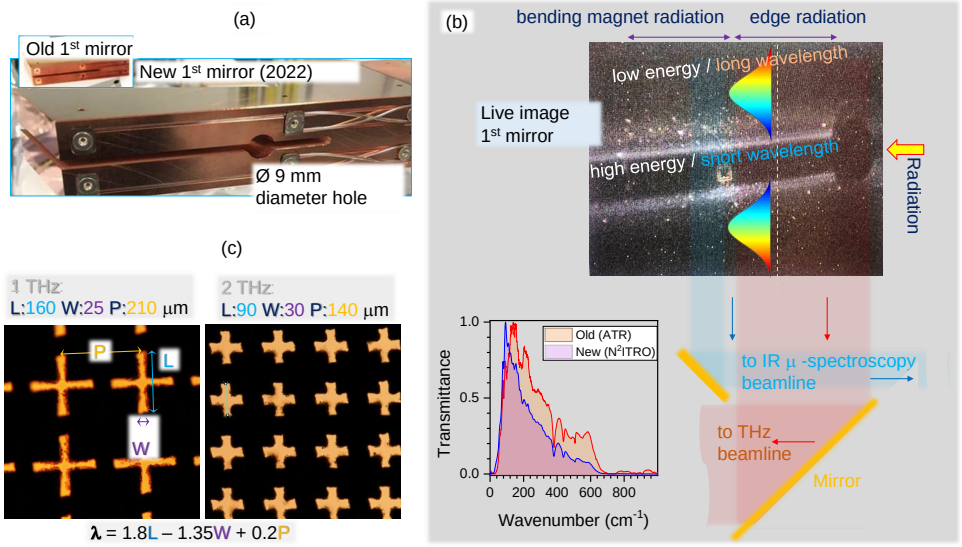

FIG. 1. (a) Photo of the newly installed first-mirror to extract IR-THz radiation out of storage ring at the AuSy (in use from Jan. 2022). (b) Video camera feed of the 1st mirror with schematics of radiation split between two beamlines; visible light (part of synchrotron radiation) is apparent at the edges of the mirror. Normalised transmittance before and after 1st mirror change is shown for the ATR and N^{2}ITRO modes, respectively (a Mylar 6 μm beamsplitter was used; see Supplement Fig. S1). (c) Optical micro-images of 1 and 2 THz filters laser ablated out of 20-μm-thick stainless steel SUS304; L, W, P are the length, width, and period of the cross-pattern.

Preprints (www.preprints.org) | NOT PEER-REVIEWED | Posted: 4 July 2022 doi:10.20944/preprints202207.0043.v1

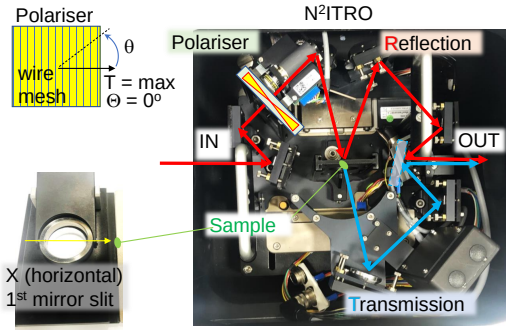

FIG. 2. Beam tracing in the Near-Normal Incidence Transmission and Reflection Optics (N^2ITRO, Bruker) unit with a step-motor controlled linear polariser. Measurements were carried out in vacuum $\sim 10^{-5}$ atm with the fabricated filters placed at the sample holder. Polariser position for maximum transmittance T was set as $\theta = 0°$.

effects of radiation on tissues as well as changes of spectral properties of biological samples upon water freezing[7–10]. The characterisation of biological tissue properties that are needed for diagnostic applications will also be aided by the availability of a narrow band filters.

Here we show a simple method to prepare such THz filters out of Kapton (polyimide) and stainless steel micro-thin foils. Filters were characterised using reflection and transmission at the THz beamline at the Australian Synchrotron (AuSy).

II. SAMPLES AND METHODS

A. Laser cutting of filters

The cross-shaped apertures were fabricated by femtosecond laser ablation cutting. This consisted of a 10 W average power PHAROS laser (Light Conversion Ltd.) coupled with a three-axis positioning stage controlled by SCA software and integrated with a 3D laser machining station (Workshop of Photonics, Ltd.). Two materials were used to fabricate the filters: $d = 25$ μm-thick SUS304 stainless steel foil (Jianglin Steel Corporation PTE Ltd.) and 25 μm-thick Kapton (polyimide derived from pyromellitic dianhydride and 4,4-oxydianiline; Du PontToray, Co., Ltd.[11]). The laser beam was scanned multiple times along the contour line of the each cross until each was completely cut through. The main parameters of the laser system were the following: the laser wavelength, pulse duration, pulse energy and repetition rate: $\lambda = 1030$ nm, $t_p = 230$ fs, $E_p = 50$ μJ/pulse laser (on the sample) and $f_p = 200$ kHz, respectively. Additionally, the scanning speed was set at $v_s = 50$ mm/s. A vacuum suction nozzle was positioned close to the cutting area to remove ablated particles and the cutout cross pieces. For the SUS304 foil it took 6 passes to completely cut through, while for the Kapton only 3 passes were required at half the pulse energy, 25 μJ/pulse. The focal position was placed on the surface of the sample and wasn't changed for subsequent passes.

The numerical aperture of the objective lens (Mitutoyo) was $NA = 0.26$, which focused the laser beam to a $2r = 1.22\lambda/NA = 4.8$ μm focal spot. Depth of focus can be estimated as double the Rayleigh length $2z_R = 2\frac{\pi r^2}{\lambda} = 35.6$ μm, which is larger than the thickness of the samples. The pulse fluence was $F_p = E_p/(\pi r^2) = 272.5$ J/cm^2 (for pulse of 50 μJ), which is more than 10^3 times the laser ablation threshold of metals at ~ 0.1 J/cm^2. The pulse average intensity $I_p = F_p/t_p = 1.19$ PW/cm^2 (ablation threshold of metal ~ 0.4 TW/cm^2). This is a high irradiance and hard X-ray generation takes place in the plasma region of the target due to bremsstrahlung[12]. When targets with heavy elements, e.g., metal targets

Preprints (www.preprints.org) | NOT PEER-REVIEWED | Posted: 4 July 2022 doi:10.20944/preprints202207.0043.v1

are used, hard X-ray generation can be significant[13,14]. It was shown that the personal exposure dose rate was $\dot{H}(0.07)$ [mSv/h/W], which saturates for the stainless steel targets at an irradiance of 0.1 PW/cm^2 with different pulse duration but using comparable exposure conditions as in our study[15]; the depth $d_p = 0.07$ mm. At an $f_p = 200$ kHz repetition rate and scanning speed of $v_s = 50$ mm/s, the pulse-to-pulse distance is $d_{pp} = v_s/f_p = 250$ nm or 5.2% of the focal diameter $2r = 4.8$ μm. This corresponds to a strong overlap between adjacent pulses.

Due to a large area fabrication 5×5 mm^2, plane fitting helps to keep the focal spot on the surface of the sample during long laser cutting times. First, coordinates of focal spot $P_i(x_i, y_i, z_i)$ on the surface of sample are determined at three corners of the write field; $i = 1 \ldots 3$. Two vectors $\overrightarrow{P_1P_2} = (x_2-x_1, y_2-y_1, z_2-z_1)$ and $\overrightarrow{P_1P_3} = (x_3-x_1, y_3-y_1, z_3-z_1)$ are in the plane and the normal to the plane is:

$$\overrightarrow{P_1P_2} \times \overrightarrow{P_1P_2} = \begin{vmatrix} \vec{i} & \vec{j} & \vec{k} \\ x_2 - x_1 & y_2 - y_1 & z_2 - z_1 \\ x_3 - x_1 & y_3 - y_1 & z_3 - z_1 \end{vmatrix} = \langle a_n, b_n, c_n, \rangle. \quad (1)$$

The plane through the point P_1 (also P_2 and P_3) is $a_n(x-x_1)+b_n(y-y_1)+c_n(z-z_1) = 0$. This is the plane equation which will account for the actual tilt. During laser writing, for the each new point $P_{new}(x_{new}, y_{new})$ along writing trajectory, the height z_{new} is calculated from the plane equation given above. The plane fitting method keeps the focal spot on the surface of sample when there is an uniform tilt. Such tilt compensation methods are implemented in direct write lithographies, e.g., electron beam lithography. For large area fabrication, the sample-focus position can drift over time. It is possible to repeat the described procedure when required manually or automatically when the intensity of back-reflected light is monitored. In the future, surface mesh leveling can be used to maintain the focal spot over a larger area by taking into account the surface topology.

In case of the filters made out of Kapton, the cross mesh pattern was coated with 20 nm-thick chromium and 50 nm-thick gold. This thickness is close to the skin depth, which reduce intensity of THz radiation by $1/e$-times (detailed discussion in Sec. III B).

B. Near-normal incidence transmission and reflection measurements

In order to determine optical properties of THz filters, measurements of reflected and transmitted intensities, I_R and I_T respectively, were made from exactly the same position on each filter. This was possible with the use of a near-Normal Incidence Transmission and Reflection Optics (N^{2}ITRO, Bruker) unit (Fig. 2). The diameter of THz beam on the sample was ~ 2 mm (Fig. S3).

Measurement of transmittance $T = \frac{I_T}{I_0}$ and reflectance $R = \frac{I_R}{I_0}$ were measured from the same spot on the filter at a selected polarisation angle θ; I_0 is the incident THz intensity. Following energy conservation, the absorptance $A = 1 - R - T$. We determined the optical density OD of the composite films with the following expression $T = (1 - R) \times 10^{-OD}$, where R and T were directly measured; also $A = (1 - R) \times (1 - 10^{-OD})$. Strong absorption conditions, when $\alpha d > 1$, is defined by the absorption coefficient α [cm^{-1}] and thickness d as $\alpha d = \ln(10)OD \equiv 2.303 \times OD$.

The lesser explored spectral region at 0.1-1 mm (100-10 cm^{-1}, 3-0.3 THz) wavelengths was selected for measurements and band-pass filters (usually, a Globar source is used in table-top FTIR spectrometers for measurements at wavenumbers larger than $\tilde{\nu} > 400$ cm^{-1}). Due to strong interference in the 120 μm Mylar beam splitter, the low intensity regions have higher $T(\tilde{\nu})$ and $R(\tilde{\nu})$ spectra (Fig. S1).

The reflectance $R = [(n-1)^2 + \kappa^2]/[(n+1)^2 + \kappa^2]$ at normal incidence to an air/vacuum interface and the complex refractive index of the sample is $\tilde{n} = n + i\kappa$. Lower reflectance R contributes to higher absorptance $A = (1 - R) \times (1 - 10^{-OD})$.

With the portions of reflected R and transmitted $T = (1 - R)10^{-OD}$ light(energy), the absorbed portion is determined $A = (1-R)(1-10^{-OD})$; the energy conservation $A+R+T =$

Preprints (www.preprints.org) | NOT PEER-REVIEWED | Posted: 4 July 2022 doi:10.20944/preprints202207.0043.v1

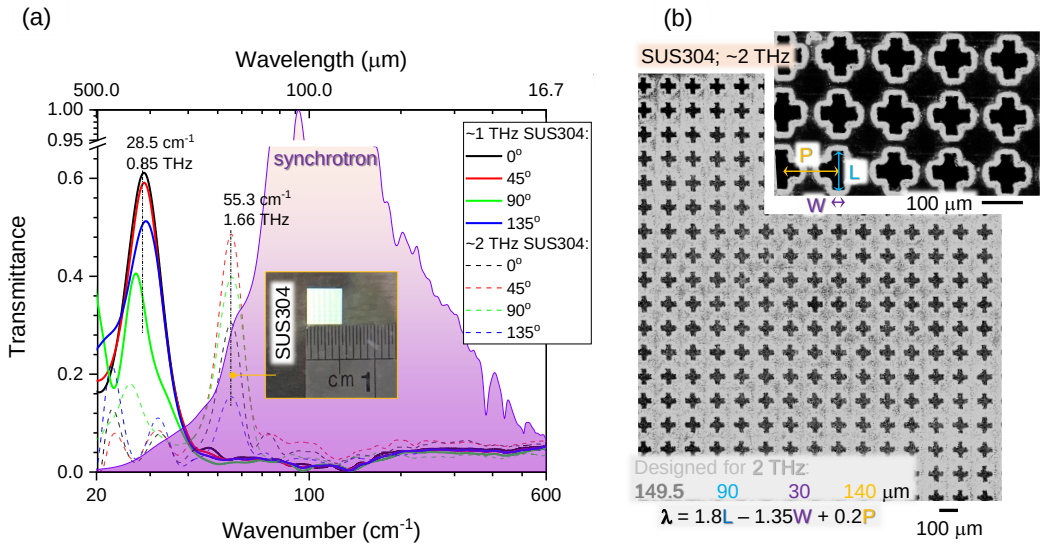

FIG. 3. THz filters made out of 25-μm-thick stainless steel SUS304. (a) Transmittance spectra at four polarisation angles for ∼1 and ∼2 THz filters. The background shows normalised AuSy spectra (with the Mylar 6 μm beamsplitter used for detector). (b) SEM images of ∼2 THz filter.

1 holds. Hence, the absorption coefficient $\alpha = 4\pi\kappa/\lambda$ (for intensity) can be determined, with both the complex refractive index and permittivity (dielectric susceptibility ε) related with $\sqrt{\varepsilon} = n + i\kappa$. With n and κ determined, the response of material at the chosen wavelength is known. For bulk material (not film) with no transmission, i.e. $T = 0$, $A = 1 - R = 2\kappa^2/[(n+1)^2 + \kappa^2]$ since $R = [(n-1)^2 + \kappa^2]/[(n+1)^2 + \kappa^2]$.

III. RESULTS AND DISCUSSION

A. Cross-filters out of metal foil

Band-pass filters are essential for determining the absorption effect at specific wavelengths. The scaling for the design of such binary transmission filters, where the central wavelength is defined by period P, width of opening W, and length of cross opening L as $\lambda_c = 1.8L - 1.35W + 0.2P$, is established[2]. For filters aimed at a low wavenumber spectral range (0.3-3 THz), all dimensions (W,L, and P) are within 10-to-100 μm. Direct laser writing based on ultra-short laser pulses was used to cut the openings in micro-films of stainless steel SUS304 and Kapton used in this study (Fig. 1(c)).

Figure 3 shows the spectral performance (a) and detailed structure (b) of the filters cut from SUS304 foil. Both, 1 and 2 THz filters as designed, showed transmission localised at slightly lower frequencies of 0.85 and 1.66 THz, respectively. The most sensitive term defining $\lambda_c = c/\nu_c$ is $1.8L$. The finite width of the laser cut increases the length of the opening, causing larger λ_c (smaller frequency ν_c). The cross-shape filters were expected to be independent on polarisation of incident THz beam, however, a clear dependence of transmission on the polarisation was observed. Each transmission spectrum was normalised to the spectrum without sample, while reflectance spectra were normalised to reflection of an Au-mirror. It is important to note that, each peak in the transmission spectra coincided with a dip in reflectance as expected (not plotted to avoid clutter). Both T and R show significant dependence on the beam polarisation; this suggests that each individual spectra should be measured as references to decouple material dependent and radiation dependent

Preprints (www.preprints.org) | NOT PEER-REVIEWED | Posted: 4 July 2022 doi:10.20944/preprints202207.0043.v1

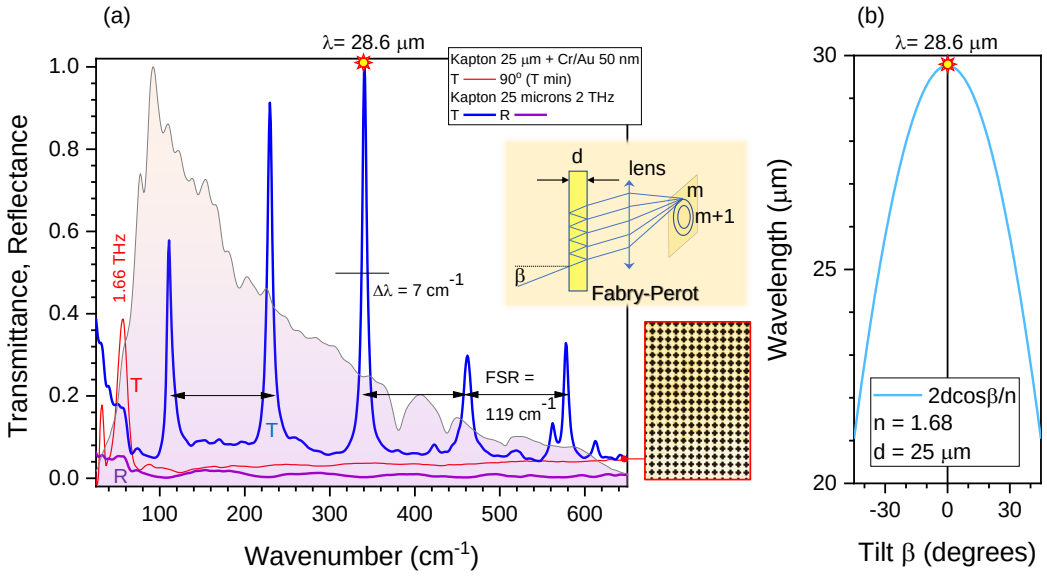

FIG. 4. THz transmission and reflection studies using Kapton filters. (a) Transmission spectra show that metal-coated Kapton was performing equivalently to the SUS304 foil filters. Kapton with cut out crossed but without coating showed Fabry-Pérot (FP) etalon action with free spectral range $FSR = 119$ cm^{-1}; this was also observed with unstructured Kapton films. The background spectra is synchrotron radiation (detected without sample, filter nor polariser). Optical image of the metal-coated filter is shown on the right-side. The inset shows schematics of the FP etalon action. (b) Tunability of FP etalon by tilt angle β for the $d = 25$ μm thick Kapton film with $n = 1.68$ refractive index. The condition of FP maxima is $2d\cos\beta = m\lambda$.

effects. The polarisation distribution over the focal spot is not uniform as was revealed in a previous inspection (see Supplement). The isotropic edge component and linear dipole parts of radiation are present and reflected from a two-lobed mirror, which fills the focal volume with different spectral components directed along slightly different wavevectors and having isotropic and linear polarisations.

B. Cross-filters and Fabry-Pérot etalon out of Kapton film

Simple and fast laser cutting of the required cross-shapes was made out of a 25-μm-thick Kapton film. The film was coated with 20 nm of Cr and 50 nm of Au to make a binary transmission mask. A very similar transmission to SUS304 filters was confirmed (Fig. 4). This shows that there were no geometrical difference in the definition of the cut width and edge quality between very different materials. The complexity of polarisation and wavelength distribution might be contributing to lower transmittance due to strong diffraction. The ratio of open area per unit cell of the pattern is $R_A = Open/Cell = (2LW - W^2)/P^2 = 23\%$ for the ~ 2 THz filter design.

The skin depth for EM radiation in an absorbing conductive coating can be estimated from $\delta_s \equiv 1/\alpha = \sqrt{\frac{2\rho}{\omega\mu}}$ when $\nu \ll \frac{1}{\rho\epsilon}$ and $\delta_s \approx 2\rho\sqrt{\frac{\epsilon}{\mu}}$ when $\nu \gg \frac{1}{\rho\epsilon}$, where $\epsilon = \epsilon_0\epsilon_r$ is the permittivity of the coating, $\mu = \mu_0\mu_r$ is its permeability, ρ [Ωm] is the resistivity, $\omega = 2\pi\nu$ is the cyclic frequency of light, ϵ_0, μ_0 are the permittivity and permeability of free space, respectively. For Cr $\rho_{Cr} = 13 \times 10^{-8}$ [Ωm] or Au $\rho_{Au} = 2.24 \times 10^{-8}$ [Ωm] with $\epsilon_0 = \frac{1}{\mu_0 c^2} = 8.85 \times 10^{-12}$ [F/m] and $\epsilon_r = \tilde{n}^2$, the $\nu = (1 - 10)$ THz frequencies are always smaller than $1/(\rho\epsilon)$. Hence, the skin depth at which intensity of light is reduced $1/e^2 = 7.4$-

Preprints (www.preprints.org) | NOT PEER-REVIEWED | Posted: 4 July 2022 doi:10.20944/preprints202207.0043.v1

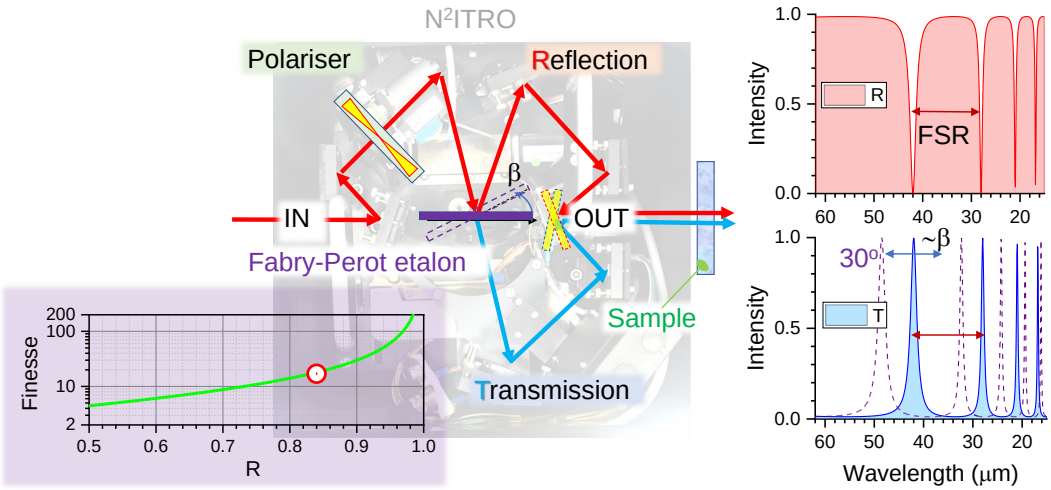

FIG. 5. Concept of $T\&R$ spectral analysis at broad and narrow spectral ranges using angular tunable FP etalon ($thickness = d/\cos\beta$) at tilt angle β using N^{2}ITRO. The T, R spectra calculated for $d = 25$ μm and refractive index $n = 1.68$ as in experiments with Kapton FP etalon; reflectivity was taken as $R = 0.8$. Finesse expression for $F_c > 0.5$ is defined as $F_c \approx \pi\sqrt{R}/(1-R)$ where R is the reflectivity of Kapton/vacuum surface. In experiments, the finesse was $F_c \approx 17$, i.e., $R = 84\%$ (a dot-marker). Transmittance spectra at tilt angle of FP etalon $\cos\beta \equiv \cos 30°$ is shown. Note, FSR is not equally spaced in wavelength and equally spaced in energy (or wavenumber $\tilde{\nu}$) since $\lambda \propto 1/\nu$.

times is defined by $\delta_s = \sqrt{\frac{2\rho}{\omega\mu}} = \frac{503}{\sqrt{\mu_r \nu \sigma}}$ where conductivity $\sigma = 1/\rho$ [S/m] and $\mu_r = 1$ for non magnetic materials, e.g., gold. For gold at $\nu = 1$ THz, one would find $\delta_s = 75$ nm and for 10 THz $\delta_s = 24$ nm. Chromium is antiferromagnetic below 38°C and for an estimate we consider $|\mu_r| \sim 1$, which yields in $\delta_s \approx 181$ nm (1 THz) and 57 nm (10 THz). We used Cr/Au:20 nm/50 nm coating on Kapton, which is close to the skin depth at several THz frequencies.

When a non-coated Kapton filter (original film) was inserted into the beam (sample in N^{2}ITRO unit), clear Fabry-Pérot (FP) etalon action was observed (Fig. 4) with a free spectral range of $FSR = 119$ cm^{-1} as defined by $d = 25$ μm thickness of the Kapton film. The ratio of FSR to the bandwidth $\Delta\lambda = 7$ cm^{-1} defines the finesse F_c, which is also the number of wavelengths which can be resolved by FP etalon $F_c = FSR/\Delta\lambda_c = 17$ at this THz spectral range. From the known thickness of Kapton $d = 25$ μm and $FSR = \frac{1}{2nd}$ cm^{-1} $= \frac{\lambda^2}{2nd}$ nm $= \frac{c}{2nd}$ Hz, one finds the refractive index of Kapton $n = 1.68$. By changing the thickness of the Kapton film, the bandwidth $\Delta\lambda \propto 1/d$ can be changed. Spectral positioning of the FP resonances can be tuned by tilt angle β of the FP etalon according to $2d\cos\beta = m\lambda_c$, where the m is order parameter (an integer); see inset in Fig. 4(a) and (b). It can be efficient to use FP etalon as a wavelength selection filter, especially for selective energy delivery to a sample by absorption. Indeed, $\Delta\lambda = 7$ cm^{-1} at $\lambda_c = 350$ cm^{-1} comprises only 2% bandwidth, which is smaller by approximately one order of magnitude as compared to cross-filters. Since higher orders of FP etalon converge towards the centre of the detector, it is a welcoming feature since it is less sensitive to beam alignment. The interference which caused the FP maxima was 1.47 times larger than the normalised transmission $T = 1$ due to constructive addition of FP modes. It is noteworthy that $R \to 0$ at the $T \to max$ (Fig. 4(a)), a tendency recognisable in the experiment.

Preprints (www.preprints.org) | NOT PEER-REVIEWED | Posted: 4 July 2022 doi:10.20944/preprints202207.0043.v1

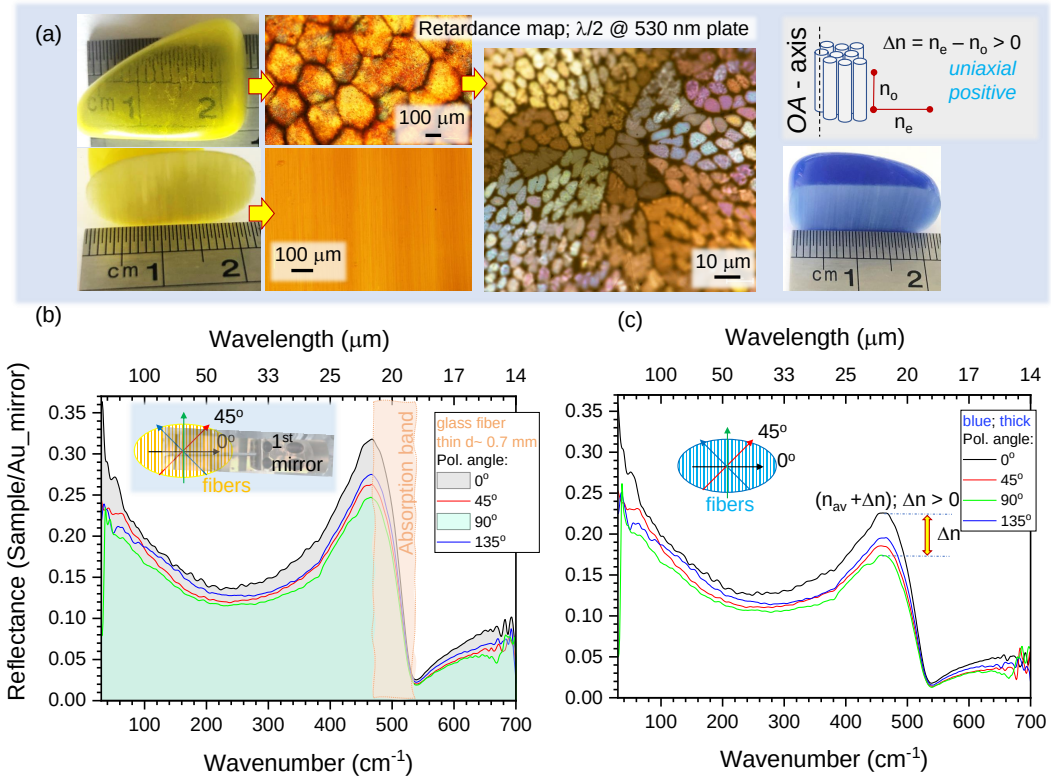

FIG. 6. (a) "Cat-eye" silica fiber stone samples. Microscopy images were taken using cross Nicol polarisers with a $\lambda/2$ plate oriented at $\pi/4$ to the crossed polarisers; plate was for 530 nm wavelength to color render the retardance. Reflectance spectra measured with N^{2}ITRO from silica-fiber "cat-eye" stones: yellow (a) and blue (b), which have form birefringence corresponding to the positive birefringence $\Delta n \equiv n_e - n_o > 0$ classified as the uniaxial postive crystal. Input polarisation was set linear at four angles $0, \pi/4, \pi/2$, and $3\pi/4$. Inset in (b) shows orientation of polarisation in respect to the slit in the first mirror. Anomalous dispersion at the absorption band is clearly discerned.

C. Concept of tunable THz filters

Figure 5 shows the concept of using the N^{2}ITRO unit as a tunable filter when the FP etalon is inserted into the sample's position at a controlled tilt angle β. The effective thickness of the FP etalon ($d = 25$ μm Kapton in this study) becomes larger with tilt $d/\cos\beta$, which tunes the phase delay $\delta = 2\pi nd/\lambda$. The transmission and reflection coefficients of the FP etalon are dependent on the reflectivity R of the FP film interfaces (both interfaces are assumed to have the same reflectivity) and FP transmittance and reflectance spectra are given by $T = \frac{(1-R)^2}{(1-R)^2+4R\sin^2\delta}$, $R = \frac{4R\sin^2\delta}{(1-R)^2+4R\sin^2\delta}$, respectively (Fig. 5). The FP etalon imparts its absorbance spectrum onto the synchrotron radiation, but using the N^{2}ITRO geometry allows the same ~ 2 mm diameter point to be probed in R and T. A sample's absorbance can be measured under broad-band R and narrow-band T excitation. Since polymer films of few micrometer thickness are readily available (e.g., 4-μm-thick ultralene), the $FSR \propto 1/d$ can be considerably increased from the 119 cm^{-1} which was for $d = 25$ μm Kapton film.

 doi:10.20944/preprints202207.0043.v1

D. Polarisation analysis of Reflectance spectra

The N^{2}ITRO unit is useful for measurements of optically thick samples ($T \to 0$) in reflection. Such a measurement is more sensitive to the real part of refractive index n since $R = [(n-1)^2 + \kappa^2]/[(n+1)^2 + \kappa^2]$ at normal incidence to an air/vacuum interface and $\tilde{n} = n + i\kappa$ being the complex refractive index of the sample. This is compared to absorbance $A = 1 - R = 2\kappa^2/[(n+1)^2 + \kappa^2]$ when $T = 0$. To test this spectral property, samples were prepared from a thermally fused bundle of optical silica fibers, which are available as chatoyant "cat-eye" souvenir silica stones (Fig. 6(a)); color pigments are added to the bundle before melting to stain the stones, however, the central silica core remains transparent and colorless. The as-cut and as-polished samples were mounted into the N^{2}ITRO holder with vertical alignment (along the y-axis; perpendicular to the 1st-mirror slit along the x-axis; Fig. 2).

Strong polarisation dependence of reflectance R was observed with clear dispersion-like spectral lineshape around the Si-O-Si symmetric bending band at 480 cm^{-1}.[16] Interestingly, this is the exact spectral position of the characteristic feature in Raman scattering spectra of silica glasses, which is understandable since scattering is sensitive to the refractive index. Since measurements were carried in reflection, which is more sensitive to the refractive index, the form birefringence of optical fibers dominates the spectral lineshape. Reflectance changed $\sim 5\%$ for spectra along and across silica fibers at the most sensitive part of spectrum near the absorption band, however, anisotropy of R was present over the entire THz spectral window. Birefringence as an anisotropy in refractive index is revealed in reflectance spectra of the sample with aligned fiber pattern. When direct transmission cannot be measured (a thick sample) and when there is no dichroism in the sample, it is still possible to reveal anisotropy in material distribution (fibers in this study) since by definition the refractive index is proportional to the mass density. It was critical to normalise each R spectra to the background measured with an Au mirror at the same input polarisation, since polarisation and wavelength distribution over the illumination area is complex (Fig. S3). For glass refractive index $n \approx 2.5$ at THz spectral window (see discussion of Fig. S4(b) in Supplement), reflection coefficient is $R = \frac{(n-1)^2}{(n+1)^2} \approx 18.4\%$ and an increase of n by $\Delta n = 0.25$ would cause $R = 21.8\%$, close to the experimental observation (Fig. 6). It is shown here that form-birefringence can be recognised at the THz spectral range from subtle changes in Refectance over a spectrally broad spectral region where absorption bands are absent. Also, dispersion-like spectral lineshapes identifies related absorption bands and can be revealed by polarisation sensitive R measurements (Fig. 6).

IV. CONCLUSIONS AND OUTLOOK

THz filters with a bandwidth of $\Delta\lambda/\lambda_c \sim 10\%$ can be made by laser cutting patterns of crosses in metals or polymer foils. Coating ~ 100 nm of metal onto polymers corresponds to skin depth and renders them optically opaque. Laser cutting of micro-films can be made with high throughput using low-NA focusing with a ~ 5 μm diameter focal spot. Such filters have low $T < 5\%$ transmittance over a wide range of wavelengths 10 μm - 0.5 mm (IR-THz). The high laser intensity ~ 1 PW/cm^2/pulse used for ablation cutting of THz filters reduces fabrication time, which can become an important factor due to hard X-ray radiation emitted from the plasma region[15]. With the increase in average power of ultra-short lasers equivalent to Moore's law[17], direct laser writing is becoming not only a propotyping tool but a high throughput industrial fabrication technique[18].

We show that Kapton films of tens-of-μm thickness perform as FP etalons. By using different film thicknesses and controlling tilt with respect to the normal incidence, the possibility to tune wavelength over absorption bands of samples with high versatility can be realised. Reflection and transmission spectra from the FP etalon can both be used for spectral characterisation using the N^{2}ITRO type setup as proposed in this study (Fig. 5).

The polarisation and intensity distribution of the synchrotron THz beam is complex.

With a characterised lateral distribution of polarisation components it would be possible to define a diffractive optical element for uniform mixing of polarisation and intensity over the focus, similar to what has been demonstrated for the optical spectral range[19]. Another solution for a more uniform distribution of polarisation over the focal region could be realised using a circular polariser based on total internal reflection in Fresnel rhomb. The average refractive index of Teflon directly measured by THz time domain spectroscopy (TDS) is $n = 1.48$ and can be easily integrated into THz beamline at AuSy.

ACKNOWLEDGMENTS

This work was supported by EU18993 2022/2 beamtime application. We are grateful to Dr. David Farrant (CSIRO, Sydney) for opportunity to take THz camera images of the focal region. The mesh-filters were fabricated by Dr. Juozas Miškinis, Vilnius University. We are grateful to Workshop of Photonics Ltd., Lithuania for fs-laser fabrication setup acquired via a technology transfer project in 2012. We thank Drs. Jonathan Tollerud and An Le, Swinburne, for setting up TDS measurements.

[1] R. Ulrich, "Interference filters for the far infrared," Appl. Opt. **7**, 1987–1996 (1968).
[2] M. Tarasov, V. Gromov, G. Bogomolov, E. Otto, and L. Kuzmin, "Fabrication and characteristics of mesh band-pass filters," Instruments & Experimental Techniques **52**, 74–78 (2009).
[3] A. Melo, M. Kornberg, P. Kaufmann, M. Piazzetta, E. Bortolucci, M. Zakia, O. Bauer, A. Poglitsch, and A. Alves da Silva, "Metal mesh resonant filters for terahertz frequencies," Appl. Opt. **47**, 6064–6069 (2008).
[4] D. Porterfield, J. Hesler, R. Densing, E. Mueller, T. Crowe, and R. Weikle, "Resonant metal-mesh band-pass filters for the far infrared," Appl. Opt. **33**, 6046–6052 (1994).
[5] R. Meguya, S.-H. Ng, M. Han, V. Anand, T. Katkus, J. Vongsvivut, D. Appadoo, Y. Nishijima, S. Juodkazis, and J. Morikawa, "Polariscopy with optical near-fields," Nanoscale Horizons , (in press) (2022).
[6] M. Ryu, D. Linklater, W. Hart, A. Balcytis, E. Skliutas, M. Malinauskas, D. Appadoo, Y. Tan, E. P. Ivanova, J. Morikawa, and S. Juodkazis, "3D printed polarizing grids for IR-THz synchrotron radiation," J. Opt. **20**, 035101 (2018).
[7] J.-B. Perraud, J.-P. Guillet, O. Redon, M. Hamdi, F. Simoens, and P. Mounaix, "Shape-from-focus for real-time terahertz 3D imaging," Opt. Lett. **44**, 483–486 (2019).
[8] Z. Vilagosh, N. Foroughimehr, A. Lajevardipour, D. Appadoo, S. Juodkazis, and A. W. Wood, "Estimating dielectric parameters by reflecting evanescent waves at THz frequencies," in *In Terahertz, RF, Millimeter, and Submillimeter-Wave Technology and Applications XV (Vol. 12000* (SPIE, 2022) pp. 126–131.
[9] M. Ryu, S. Ng, V. Anand, S. Lundgaard, J. Hu, T. Katkus, D. Appadoo, Z. Vilagosh, A. Wood, S. Juodkazis, and J. Morikawa, "Attenuated total reflection at thz wavelengths: Prospective use of total internal reflection and polariscopy," Applied Sciences **11**, 7632 (2021).
[10] D. J. Segelstein, *The complex refractive index of water* (Doctoral dissertation, University of Missouri–Kansas City, 1981).
[11] J. Morikawa, A. Orie, T. Hashimoto, and S. Juodkazis, "Thermal diffusivity in femtosecond-laser-structured micro-volumes of polymers," Appl. Phys. A. **98**, 551–556 (2010).
[12] H.-H. Huang, T. Nagashima, W.-H. Hsu, S. Juodkazis, and K. Hatanaka, "Dual THz wave and X-ray generation from a water film under femtosecond laser excitation," Nanomaterials **8**, 523 (2022).
[13] K. Hatanaka, T. Ida, H. Ono, S.-I. Matsushima, H. Fukumura, S. Juodkazis, and H. Misawa, "Chirp effect in hard X-ray generation from liquid target when irradiated by femtosecond pulses," Opt. Express **16**, 12650–12657 (2008).
[14] W. H. Hsu, F. C. P. Masim, M. Porta, M. T. Nguyen, T. Yonezawa, A. Balčytis, X. Wang, L. Rosa, S. Juodkazis, and K. Hatanaka, "Femtosecond laser-induced hard X-ray generation in air from a solution flow of Au nano-sphere suspension using an automatic positioning system," Opt. Express **24**, 19994 – 20001 (2016).
[15] J. Holland, R. Weber, M. Sailer, and T. Graf, "Influence of pulse duration on X-ray emission during industrial ultrafast laser processing," Materials **15**, 2257 (2022).
[16] T. Uchino, A. Aboshi, S. Kohara, Y. Ohishi, M. Sakashita, and K. Aoki, "Microscopic structure of nanometer-sized silica particles," Phys. Rev. **69**, 155409 (2004).
[17] M. Han, D. Smith, S.-H. Ng, V. Anand, T. Katkus, and S. Juodkazis, "Ultra-short-pulse lasers—materials—applications," Eng. Proc. **11**, 44 (2021).
[18] M. Malinauskas, A. Žukauskas, S. Hasegawa, Y. Hayasaki, V. Mizeikis, R. Buividas, and S. Juodkazis, "Ultrafast laser processing of materials: from science to industry," Light: Science & Applications **5**, e16133 (2016).
[19] R. Dharmavarapu, S. Bhattacharya, and S. Juodkazis, "Diffractive optics for axial intensity shaping of Bessel beams," J. Opt. **20**, 085606 (2018).

Preprints (www.preprints.org) | NOT PEER-REVIEWED | Posted: 4 July 2022 doi:10.20944/preprints202207.0043.v1

Appendix A: Polarisation map of synchrotron radiation at AuSy THz beamline

Polarisation was defined as x and y-pol. (horizontal and vertical) in room frame of reference along direction of propagation (z-axis) in the transmission mode. Data analysis was carried out with OPUS 8.0 software (Bruker Optik GmbH).

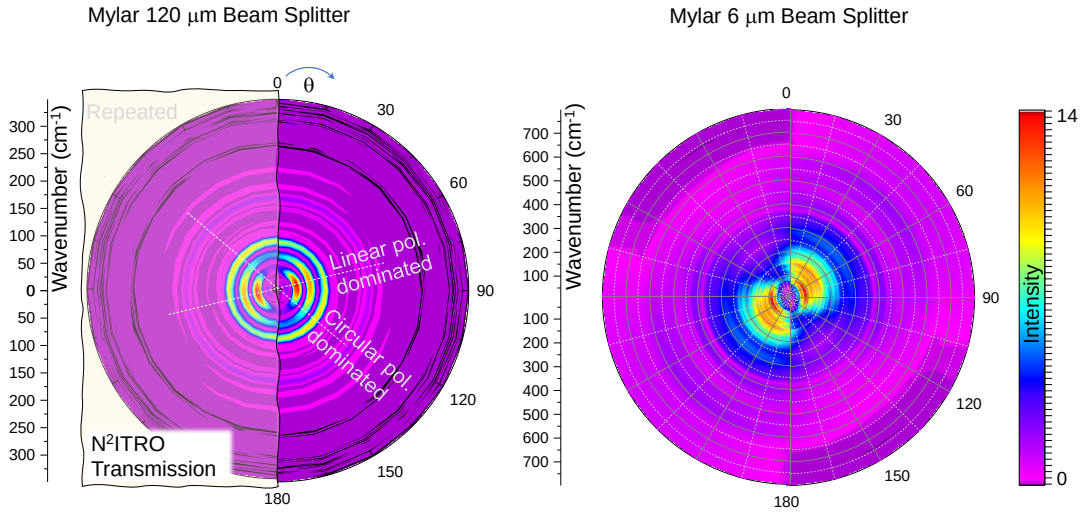

FIG. S1. Angular dependence of the narrow and broadband THz radiation with beam splitters: 120 and 6 μm Mylar, respectively, measured in transmission mode with wire mesh polariser with $\Delta\theta = 15^\circ$ steps using N^{2}ITRO unit (with no sample; see Fig. 2). Angular measurements were carrier out in the $\theta = 0 - \pi$ range and repeated to complete 2π polar plot (old 1$^{\text{st}}$ mirror).

Different Mylar beamsplitters are used to select the spectral window for measurements, tailored for broadband and narrow spectral regions at low wavenumbers $\tilde{\nu} < 50$ cm^{-1} (Fig. S1). The beamspliter is an integral part of the FTIR spectrometer and is installed before the sample compartment. For the broadest spectral characterisation of filters, the 6 μm Mylar beamsplitter was used in this study (Fig. S1).

An image of the AuSy THz beam was taken with an uncooled focal plane array (FPA) micro-bolometer camera (Microxcam 384i THz). It has a 384 $\times$ 288 resolution, 35 μm pixel size, 16-bit resolution in intensity, and a parylene-C antireflective coating. The focal length of the mounted imaging lens was $f = 44$ mm and f-number $F_\# \equiv f/D = 0.95$ ($NA = \frac{1}{2F_\#} = 0.53$ when entire aperture of diameter D is filled with THz beam).

Appendix B: Mesh-filters

The spectral band for THz spectroscopy is selected by Mylar micro-film filters (Fig. S1) at the AuSy THz beamline. Time domain spectroscopy (TDS) can be used to measure low-THz band 0.1-1 THz and was applied for characterisation of materials promising for fabrication of optical elements, filters, polarisers, and polarisation optics such as retarders and waveplates. For example, a Fresnel rhomb is a good solution for generation of circularly polarised THz emission and can be made out of Teflon.

Figure S4(a) shows optical images of a mesh used for screen printing, which can also be used as a THz filter (see T vs. $\tilde{\nu}$ plot at the inset measured at AuSy THz beamline).

Preprints (www.preprints.org) | NOT PEER-REVIEWED | Posted: 4 July 2022 doi:10.20944/preprints202207.0043.v1

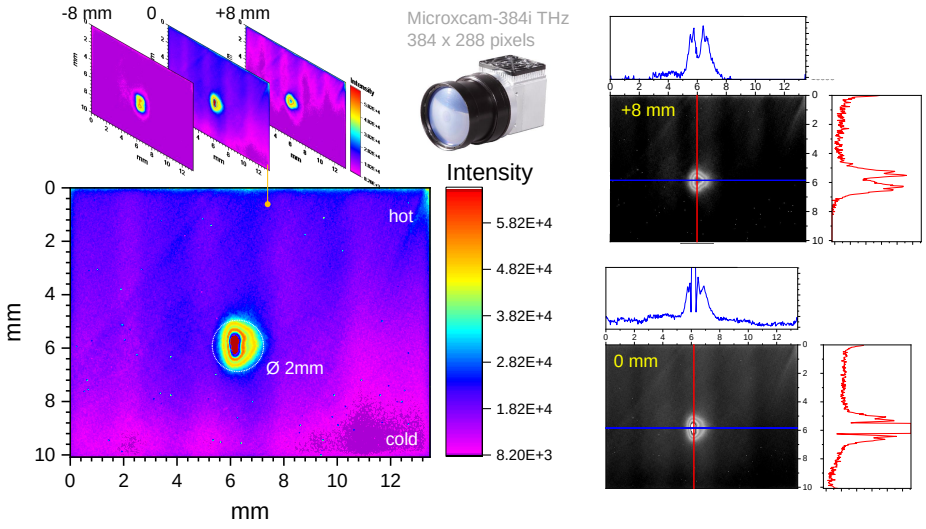

FIG. S2. Visualisation of THz beam at the focal region without spectral nor polarisation discrimination (8-bit Microxcam-384i camera). Central cross sections at 0 and 8 mm positions are shown on the right-side plots. Beam diameter at the focus was ~ 2 mm; saturation at the central 0.5 mm spot was present at the recording conditions (old 1st mirror).

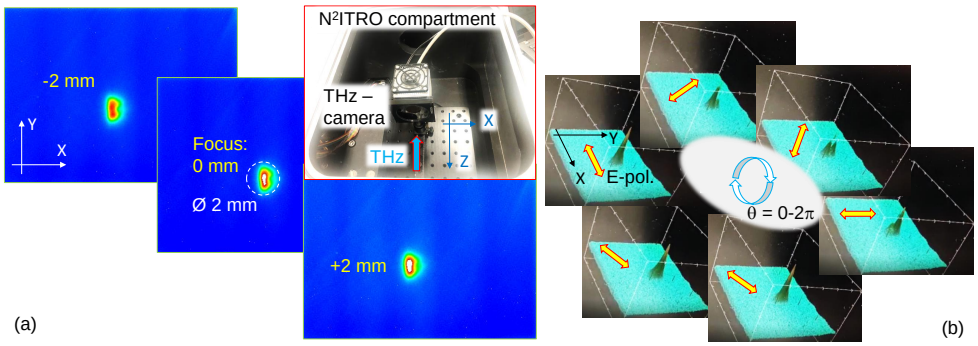

FIG. S3. Polarisation contents over the focal beam has non-uniform structure. (a) Near-focus (at -2 mm and +2 mm) images of the THz beam (AuSy) taken with Microxcam-384i camera (inset). (b) Snapshots from 3D rendering video of intensity distributions with a polariser rotating before the focus (old 1st mirror).

Ni-plated meshes were produced by: 1) diamond scribing a glass plate, then 2) plasma sputtering of Cu and 3) mechanical polishing to remove metal from the flat glass surface 4) electrochemical Ni plating on the remaining copper. The width of the metallic part was proportional to the thickness (height) of the mesh and was controlled by the deposition time. The inset in (a) shows transmittance spectra at four incident linear polarisation orientations $0, \pi/4, \pi/2,$ and $3\pi/2$, with a clear high transmission peak at ~ 80 cm^{-1} or 2.4 THz. The same mesh filter was measured using TDS at room conditions (Fig. S4(c)). Ambient water absorption is recognisable on the spectral line-shape of the filter. TDS allows direct measurement of time delay through the sample Δt and the refractive index $n = \frac{\phi_{sample} - \phi_{air}}{d \times 2\pi\nu/c} + 1 \equiv \frac{\Delta t}{d/c} + 1$, where d is the sample's thickness, ϕ is the phase of signal, ν is the frequency. For the $\Delta t = 1.6$ ps delay in $d = 1$ mm thick teflon (Fig. S4(c) inset), one finds $n = 1.480$. For slide glass $d = 1$ mm, $\Delta t = 5.2$ ps and $n = 2.56$.

 doi:10.20944/preprints202207.0043.v1

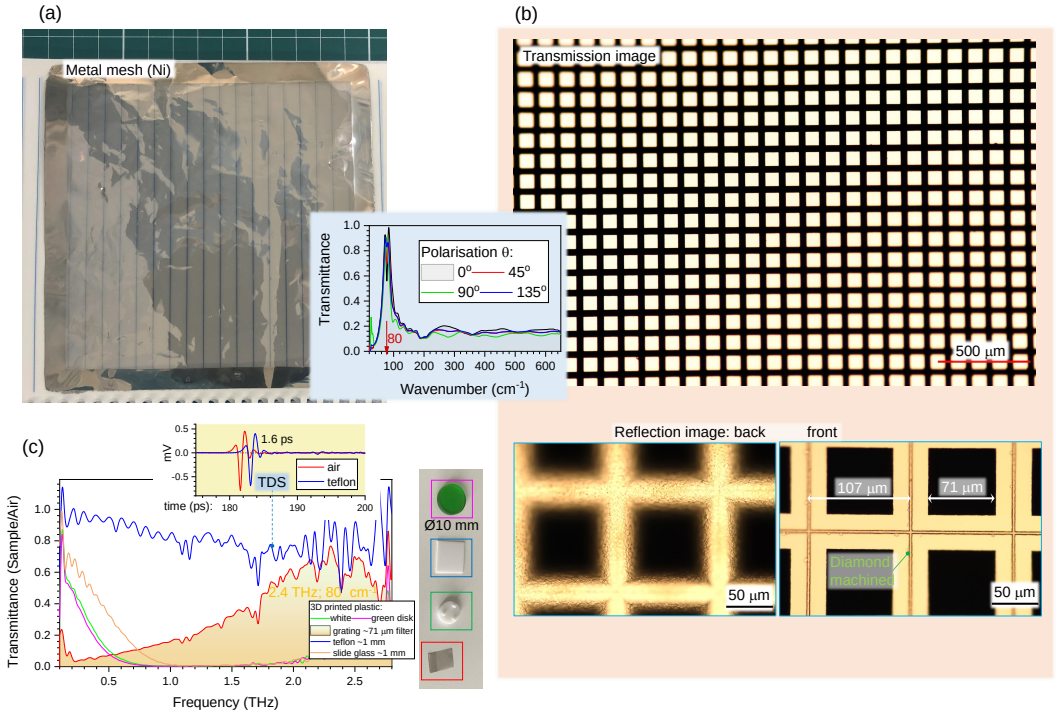

FIG. S4. (a) Ni-mesh THz filter. Background lines are from a ruled notebook. (b) Optical microscopy images of segments from 20×20 cm^2 Ni plated micro-mesh at different magnifications. Inset shows THz transmittance spectra of the ~ 2.4 THz ($\tilde{\nu} = 80$ cm^{-1}). (c) THz time domain spectroscopy (TDS; TDS10XX Batop optoelectronics) spectra (at room conditions) of several materials promising for THz optical elements. The TDS spectra reveals details at the 0.1-1 THz band. Top-inset shows time domain data for 1-mm-thick teflon which cause $\Delta t = 1.6$ ps delay as compared with air.